

**Double-ring network model of the head-direction system**Xiaohui Xie,<sup>1,\*</sup> Richard H. R. Hahnloser,<sup>1,2</sup> and H. Sebastian Seung<sup>1,2</sup><sup>1</sup>*Department of Brain and Cognitive Sciences, Massachusetts Institute of Technology, E25-210, 45 Carleton Street, Cambridge, Massachusetts 02139*<sup>2</sup>*Howard Hughes Medical Institute, Massachusetts Institute of Technology, 77 Massachusetts Avenue, Cambridge, Massachusetts 02139*  
(Received 1 June 2002; published 9 October 2002)

In the head-direction system, the orientation of an animal's head in space is encoded internally by persistent activities of a pool of cells whose firing rates are tuned to the animal's directional heading. To maintain an accurate representation of the heading information when the animal moves, the system integrates horizontal angular head-velocity signals from the vestibular nuclei and updates the representation of directional heading. The integration is a difficult process, given that head velocities can vary over a large range and the neural system is highly nonlinear. Previous models of integration have relied on biologically unrealistic mechanisms, such as instantaneous changes in synaptic strength, or very fast synaptic dynamics. In this paper, we propose a different integration model with two populations of neurons, which performs integration based on the differential input of the vestibular nuclei to these two populations. We mathematically analyze the dynamics of the model and demonstrate that with carefully tuned synaptic connections it can accurately integrate a large range of the vestibular input, with potentially slow synapses.

DOI: 10.1103/PhysRevE.66.041902

PACS number(s): 87.19.La, 87.18.Sn, 87.10.+e, 05.45.-a

**I. INTRODUCTION**

In the rat head-direction system, head-velocity inputs from the vestibular nuclei are integrated to yield a neural representation of the current directional heading with respect to the external environment. Neurons of this system, called head-direction cells, fire maximally when the rat's head faces one particular direction [1–4]. These cells usually have different preferred directions, and a population of them encodes the rat's directional heading.

Previously, several network models have been proposed to emulate the properties of head-direction cells [5–7]. The work by Zhang focuses on modeling persistent activity of head-direction cells during stationary head states [5]. The persistent neural activity is generated in a ring-attractor network with symmetric excitatory and inhibitory synaptic connections. Independently, he and Redish *et al.* showed that integration is possible by adding asymmetric connections to the attractor network [5,6]. The strength of these connections is modulated by head velocity. When the rat moves its head to the right, the asymmetric feedback loops between neurons are biased toward the right-hand side and so induce a rightward shift of the activity in the attractor network. However, using instantaneous changes in synaptic strength as the integration mechanism is biologically unrealistic. A more plausible model without multiplicative modulation of connections has been studied recently by Goodridge and Touretzky [7]. There, the head-velocity input has a modulatory influence on the firing of intermittent neurons with spatially offset connections rather than on their connection strengths. However, to achieve accurate integration in this model, the head-velocity input has to be transformed with some nonlinear function before acting on the network. This nonlinear function was obtained by curve fitting the simulation with the

desired result. It is unclear whether such nonlinear transformations actually exist in the head-direction system. Moreover, in this model, to achieve good integration for large head velocities, very fast synapses (less than 1 ms for Ref. [7]) had to be assumed.

In this paper, we present a neural integration model with two populations of neurons, following original suggestions by Zhang [5]. It integrates the head-velocity signal directly based on the differential vestibular input to these two populations, using potentially slow synapses such as N-methyl-D-aspartate (NMDA) and Gamma-aminobutyric acid type b (GABA<sub>b</sub>). In this model, the connections made by one ring are responsible for rightward turns and the connections made by the other ring are responsible for leftward turns. We mathematically analyze the dynamics of the network, and find that with carefully chosen synaptic parameters, the network is able to achieve integration with high precision.

Although our network is conceptually simpler than previous models, we show that using two simple read-out methods, averaging and extracting the maximum, it is possible to approximate head-velocity independent tuning curves observed in the postsubiculum (POS) and anticipatory responses observed in the anterior dorsal thalamus (ADT) [2,8].

**II. DEFINITION OF THE MODEL**

We model the head-direction system with two populations of neurons, each of which is organized into a ring network structure. We assume the population size in each ring is sufficiently large, so that activities of neurons sharing similar properties in each ring can be averaged, resulting in a continuous approximation of the discrete neuronal dynamics,

$$\tau \frac{\partial s_l(\theta, t)}{\partial t} + s_l(\theta, t) = f_l(\theta, t), \quad (1a)$$

$$\tau \frac{\partial s_r(\theta, t)}{\partial t} + s_r(\theta, t) = f_r(\theta, t), \quad (1b)$$

\*Email address: xhx@ai.mit.edu

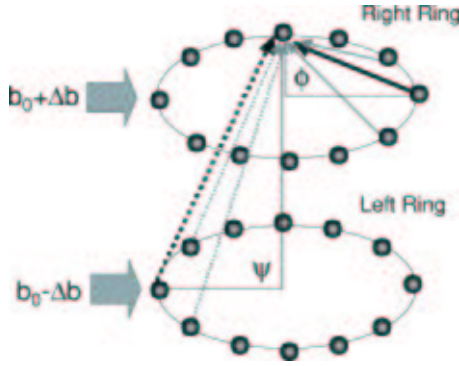


FIG. 1. A diagram of the double-ring network. Neurons in each ring receive uniform feedforward input,  $b_0 + \Delta b$  to the right ring and  $b_0 - \Delta b$  to the left ring. Neurons in each ring also receive feedback input from neurons in both the rings. Both the intraring and interring interactions are rotationally invariant and asymmetric with an offset of  $\phi$  for the intraring interaction, and  $\psi$  for the interring interaction. Illustrated in this diagram is the feedback input to a neuron in the right ring. This neuron receives the strongest input from the neuron of the same ring at the phase that is  $\phi$  smaller (solid line), and the neuron of the other ring at the phase that is  $\psi$  larger (dashed line).

which are leaky integrators that model the dynamics of synapses with time constant  $\tau$ .  $s_l(\theta, t)$  and  $s_r(\theta, t)$  represent synaptic activation (e.g., neurotransmitter concentration) indexed by  $\theta$  at time  $t$  in the left and right ring, respectively.  $f_l(\theta, t)$  and  $f_r(\theta, t)$  denote the activities of neurons in the left and right ring, respectively, which are determined by the feedforward inputs and the recurrent synaptic inputs weighted by synaptic connection strengths,

$$f_l = \left[ \int_{-\pi}^{\pi} [W_s(\theta - \theta' - \phi)s_l(\theta', t) + W_d(\theta - \theta' + \psi)s_r(\theta', t)](2\pi)^{-1} d\theta' + b_l \right]^+, \quad (2a)$$

$$f_r = \left[ \int_{-\pi}^{\pi} [W_d(\theta - \theta' - \psi)s_l(\theta', t) + W_s(\theta - \theta' + \phi)s_r(\theta', t)](2\pi)^{-1} d\theta' + b_r \right]^+, \quad (2b)$$

where  $[x]^+ \equiv \max(0, x)$  denotes the rectification nonlinearity.  $b_l$  and  $b_r$  are the vestibular feedforward inputs that differentially signal head movements with a common baseline. For simplicity, we take  $b_l = b_0 - \Delta b$  and  $b_r = b_0 + \Delta b$ , where  $\Delta \hat{b} \equiv \Delta b / b_0$  is proportional to angular head velocity. The function  $W_s$  represents the synaptic connection profile between neurons on the same ring and  $W_d$  between neurons on different rings. The phase variable  $\phi$  is the intraring connection offset and  $\psi$  is the interring connection offset. The two rings form mirror-symmetric copies of each other. A diagram of the two rings is shown in Fig. 1.

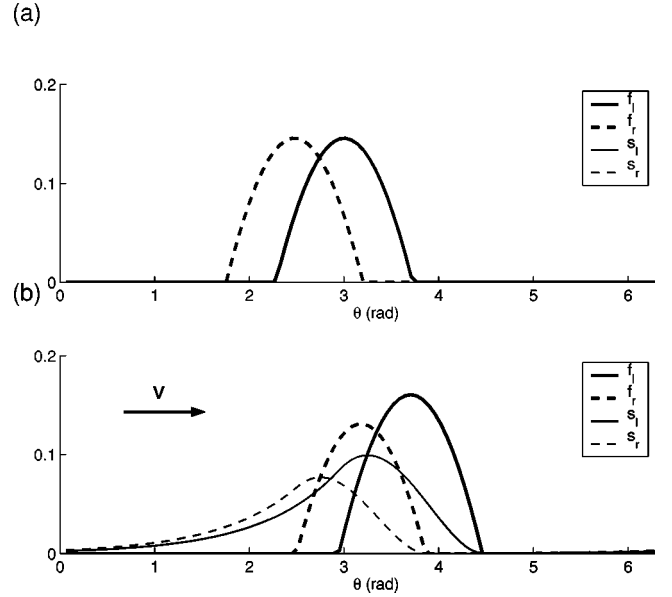


FIG. 2. Neural activity and synaptic activation profiles of two rings in the stationary (a) and the moving state (b). The dashed and solid lines correspond to the left and right ring, respectively. In Panel (a),  $s_l$  and  $f_l$  overlap with each other (because  $s_l = f_l$  when  $\Delta \hat{b} = 0$ ), so do  $s_r$  and  $f_r$ . The activities are normalized by  $b_0$  and have no units. In (a),  $\Delta \hat{b} = 0$ ; in (b)  $\Delta \hat{b} = -0.2$ . Other parameters  $J_0 = -60$ ,  $K_0 = -5$ ,  $J_1 = K_1 = 80$ ,  $\phi = 80^\circ$ ,  $\psi = 50^\circ$ , and  $\tau = 80$  ms.

Because of the rotational symmetry of the ring network structure, the functions  $W_d$  and  $W_s$  can be decomposed into sums of Fourier series. For simplicity of mathematical treatment, we approximate each of them by the first two Fourier components,

$$W_s(\theta) = J_0 + J_1 \cos \theta, \quad W_d(\theta) = K_0 + K_1 \cos \theta, \quad (3)$$

where  $J_0$ ,  $J_1$ ,  $K_0$ , and  $K_1$  are synaptic connection parameters determining the connection strength of the intraring and interring connections.

### III. INTEGRATION

Depending on the parameters chosen, the network Eq. (1) may exhibit very different dynamic behavior. We model the head-direction system with an appropriately chosen parameter regime, under which the activities in each ring converge to a stationary bump profile when  $\Delta b = 0$  [Fig. 2(a)], and generate a traveling bump with constant form when  $\Delta b \neq 0$  [Fig. 2(b)].

The stationary bump represents persistent activities of the head-direction cells when the animal is not moving. Because of the rotation symmetry of the ring network, this stationary bump can be located at any position, and thus is able to represent an arbitrary head direction. The symmetry also implies that the tuning curves of individual head-direction cells with respect to the head direction is the same as the profile of the stationary bump. Therefore, properties of the bump can

be used to predict those of the tuning curves, which can be measured in experiments by single-unit recordings.

When  $\Delta b$  is nonzero, the stationary bump starts to move with a velocity depending on  $\Delta b$ . The moving of the bump reflects the integration process. To achieve accurate integration, several requirements need to be met.

First, the angular velocity  $v$  of the traveling bump needs to be equal to the angular head velocity. In our model, we assume that  $\Delta \hat{b}$  is proportional to the head angular velocity. Therefore, for perfect integration,  $v$  needs to be linearly related to  $\Delta \hat{b}$ . Second, the linearity should extend over a large range of  $\Delta b$ . Since the vestibular input is excitatory,  $b_l, b_r \geq 0$ , we consider the range  $|\Delta \hat{b}| \leq 1$ . Third, animals can keep track of head direction even at very high head velocities (e.g., up to  $700^\circ/\text{s}$  in mice). This requires that the network be able to produce traveling bumps with high velocities. This can be easily achieved by using a fast synaptic time constant  $\tau$ . However, with slow synapses such as NMDA or GABA<sub>B</sub>, a large range, precise integration imposes constraints on the synaptic connection parameters.

Next, we analyze the dynamics of the network, and demonstrate that the above requirements on accurate integration can be achieved with carefully tuned synaptic parameters. We start by first finding stationary solutions when  $\Delta b = 0$ , and then characterize the functional relationship between  $v$  and  $\Delta b$ .

### A. Stationary solution

When the head is not moving ( $\Delta b = 0$ ), both rings receive same feedforward input. Suppose the synaptic connection parameters are chosen such that each ring forms a stationary bump, which can be written, according to the symmetry, in the form [see Fig. 2(a)]

$$\begin{aligned} s_l^*(\theta) &= [A \cos(\theta - \theta_0) - C]^+ \\ s_r^*(\theta) &= [A \cos(\theta - \theta_0 + \beta) - C]^+, \end{aligned} \quad (4)$$

where  $\theta_0$  represents the current head direction,  $\beta$  is the offset between the two bumps, and \* denotes the steady states. Substituting this equation into the steady state of Eq. (1)  $s_l^*(\theta) = f_l^*(\theta)$  and  $s_r^*(\theta) = f_r^*(\theta)$ , we derive that the parameters  $A$ ,  $C$ , and the offset  $\beta$  should satisfy

$$\beta = \arcsin(J_1/K_1 \sin \phi) - \psi, \quad (5)$$

$$A = b_0 [-(J_0 + K_0)f_0(\theta_c) - \cos \theta_c]^{-1}, \quad (6)$$

$$1 = f_1(\theta_c) [J_1 \cos \phi + (K_1^2 - J_1^2 \sin^2 \phi)^{1/2}], \quad (7)$$

where the functions  $f_0$  and  $f_1$  are given by

$$f_0(\theta_c) = \frac{1}{\pi} (\sin \theta_c - \theta_c \cos \theta_c),$$

$$f_1(\theta_c) = \frac{1}{2\pi} \left[ \theta_c - \frac{1}{2} \sin(2\theta_c) \right].$$

Here  $\theta_c$  is the critical half-width beyond which  $f_l(\theta)$  is zero, that is,  $A \cos \theta_c = C$  (The critical half-width is the same for both rings when  $\Delta b = 0$ .) The above set of equations fully characterizes the stationary bump solution. Eq. (5) determines the offset  $\beta$  between the two rings, Eq. (7) determines the threshold  $\theta_c$ , and Eq. (6) determines the amplitude  $A$ . Once  $\theta_c$  and  $A$  are known,  $C$  can be computed accordingly.

Because of the rotational symmetry inherent in the network, the stationary bump is marginally stable. Its location is not specified by the steady state equations, but rather by the initial conditions of the dynamics. The stationary bump is maintained due to the balance in the interaction received from each ring. When  $\Delta b \neq 0$ , the neural activities in one ring increase at the expense of the other ring, which causes an imbalance in the interaction between the two rings and drives the activity bump to move around. The dependence of the traveling velocity  $v$  on  $\Delta b$  is complicated because of the nonlinearity of the dynamics. However, when  $\Delta \hat{b}$  is small we can characterize the dependence of  $v$  on  $\Delta \hat{b}$  by perturbation.

### B. Small head-velocity approximation

To study the traveling bump solution with velocity  $v$ , we transform the coordinate into a moving frame attached to the bumps traveling at velocity  $v$ . After the change of variables  $S_l(\theta, t) = s_l(\theta - vt, t)$ , the original traveling bump corresponds to a stationary solution in the new coordinate, satisfying

$$\begin{aligned} -\tau v S_l^{*'}(\theta) + S_l^*(\theta) &= F_l(\theta) \\ -\tau v S_r^{*'}(\theta) + S_r^*(\theta) &= F_r(\theta), \end{aligned} \quad (8)$$

where  $F_l(\theta) = f_l^*(\theta - vt, t)$ ,  $F_r(\theta) = f_r^*(\theta - vt, t)$ , and ' denotes the differentiation with respect to  $\theta$ .

When  $\Delta \hat{b}$  is small,  $\Delta b/b_0 \ll 1$ , inside the excited regime [ $F_l(\theta) > 0$ ,  $F_r(\theta) > 0$ ], the solutions  $S_l^*(\theta)$  and  $S_r^*(\theta)$  can be viewed as perturbations of  $s_l^*(\theta)$  and  $s_r^*(\theta)$  of Eq. (4), respectively,

$$S_l^*(\theta) = (A + \delta A_l) \cos(\theta - \theta_0) - (C + \delta C_l), \quad (9)$$

$$S_r^*(\theta) = (A + \delta A_r) \cos(\theta + \beta - \theta_0) - (C + \delta C_r). \quad (10)$$

Substituting Eqs. (9) and (10) into Eq. (8) and linearizing the dynamics, we find  $v$  is determined by

$$v = J_1 \sin \phi (2\pi\tau A)^{-1} [(\theta_c + \sin(2\theta_c)/2) \delta A - 2 \sin \theta_c \delta C], \quad (11)$$

where  $\delta A \equiv \delta A_r - \delta A_l$  and  $\delta C \equiv \delta C_r - \delta C_l$ . To determine  $\delta A$  and  $\delta C$ , we linearize the dynamics of the variable  $S_r^*(\theta - \beta) - S_l^*(\theta) = \delta A \cos(\theta - \theta_0) - \delta C$ , from which we find

$$\delta A = 2[(k_3 \theta_c - 1)k_2 - k_3 \sin \theta_c]^{-1} \Delta b, \quad (12)$$

$$\delta C = 2k_2[(k_3 \theta_c - 1)k_2 - k_3 \sin \theta_c]^{-1} \Delta b, \quad (13)$$

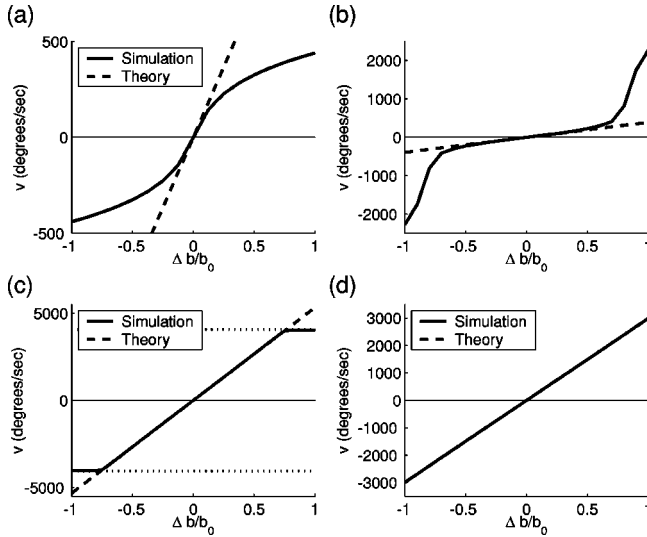


FIG. 3. Moving bump velocity  $v$  as a function of the input  $\Delta b$  for different synaptic parameters. The slope is indicated as the dashed lines. All these curves saturate when  $|\Delta b|$  is large, with the saturating velocity indicated by the dotted line. Panel (a) shows the result when  $K_1 < J_1$  ( $K_1 = 70$ ,  $\phi = 60$ ). Panel (b) shows the result when  $K_1 > J_1$  ( $K_1 = 100$ ). Linearity of the  $v - \Delta b$  curve over a wide range is achieved when  $K_1 = J_1$  as indicated in Panels (c) and (d). The range of linearity is related to the synaptic variable  $K_0$  as shown in Panel (c) for  $K_0 = -20$  and Panel (d) for  $K_0 = -5$ . If not otherwise stated, the parameters used are  $J_0 = -60$ ,  $J_1 = 80$ ,  $\phi = 80^\circ$ ,  $\psi = 50^\circ$ , and  $\tau = 80$  ms.

where  $k_1 = [J_1 \cos \phi - K_1 \cos(\psi + \beta)]^{-1}$ ,  $k_2 = [\theta_c + \sin(2\theta_c)/2 - 2\pi k_1](2 \sin \theta_c)^{-1}$ , and  $k_3 = (J_0 - K_0)/\pi$ . By substituting  $\delta A$  and  $\delta C$  into Eq. (11), we find

$$v = 2k_1 J_1 \sin \phi (\tau A)^{-1} [(k_3 \theta_c - 1)k_2 - k_3 \sin \theta_c]^{-1} \Delta b. \quad (14)$$

Equation (14) relates the velocity  $v$  of the two bumps to the differential vestibular input  $\Delta b$  when  $\Delta \hat{b} \ll 1$ . This linear  $v - \Delta b$  relationship is plotted in Fig. 3 for various synaptic parameters, and is compared with the results obtained from numerical simulations. There is a good agreement with Eq. (14) only in a small region around the origin [Figs. 3(a), 3(b)]. As we have discussed, the desired  $v - \Delta b$  curve should be linear over entire range of  $\Delta \hat{b}$  ( $|\Delta \hat{b}| \leq 1$ ). Such a large-range linear regime is shown in Fig. 3(d). In Sec. IV A we will address how to choose synaptic parameters to achieve this result.

One observation of the  $v - \Delta b$  curve is that  $v$  saturates in both ends when  $|\Delta b|$  is sufficiently large. The saturation velocity sets a limit on the largest velocity at which the bump can move. Next we calculate this saturation velocity, and discuss how to choose synaptic parameters such that the saturation velocity is sufficiently large.

### C. Saturating velocity

When  $\Delta b$  is sufficiently large, the left ring becomes inactive at some point. In this case, the network dynamics are determined only by neurons in the right ring. This still leads

to a traveling bump solution in the right ring due to the asymmetric recurrent connections. However, the traveling velocity is fixed, independent of the exact value of  $\Delta b$ , as long as it is above a threshold value. This happens because the intraring synaptic connection strength can be separated into two terms: one is symmetric and the other one is anti-symmetric as follows:

$$\begin{aligned} W(\theta) &= J_0 + J_1 \cos(\theta - \phi) \\ &= J_0 + J_1 \cos \phi \cos \theta + J_1 \sin \phi \sin \theta \\ &= \tilde{W}_S(\theta) - \tan \phi \tilde{W}'_S(\theta), \end{aligned}$$

where  $\tilde{W}_S(\theta) = J_0 + J_1 \cos \phi \cos \theta$ .

Now, let  $s^*(\theta)$  be the steady solution of a ring network with symmetric connections  $\tilde{W}_S(\theta)$ . It follows that  $s^*(\theta - \tan \phi / \tau)$  is the solution of a ring network with connections  $W(\theta)$ , which can be shown by differentiating  $s^*(\theta - \tan \phi / \tau)$ . Hence, the saturating velocity  $v_{sat}$  is given by

$$v_{sat} = \tan \phi / \tau. \quad (15)$$

To make the saturation velocity high, we can use a small synaptic time constant  $\tau$ , or choose the phase variable  $\phi$  to be close to  $\pi/2$ , which seems necessary if slow synapses are involved in the integration of the head-direction system. For the parameters used in Figs. 3(c), 3(d), we use  $\phi = 80^\circ$  and  $\tau = 80$  ms, and find  $v_{sat} = 4062^\circ/\text{sec}$ .

Similarly, when  $\Delta b$  is large negative over some threshold value, the right ring is inactivated, and the traveling bump in the left ring moves in opposite direction with the speed saturated at  $v_{sat}$  also [see Fig. 3(c)].

So far, our characterization of the  $v - \Delta b$  relationship has been based on special cases. Next, we analyze the dynamics of the double-ring network more systematically by Fourier transforming the original continuous field dynamics into one described by a set of order parameters. Based on these order parameter dynamics, we analyze the solution for traveling bumps, and discuss how to choose synaptic parameters to achieve a large linear range like the one plotted in Fig. 3(d).

## IV. ANALYSIS IN TERMS OF FOURIER MODES

The double-ring network presented here has two special properties that aid mathematical treatments. First, it is translation invariant with period  $2\pi$ . Second, the synaptic interaction function involves only the first two Fourier components. Therefore, we can simplify the original dynamics significantly by performing a Fourier transform. Next we present the analysis, following the similar treatments of Hansel and Sompolinsky [9].

Let us define the order parameters

$$r_i^0(t) = \int_{-\pi}^{\pi} s_i(\theta, t) (2\pi)^{-1} d\theta, \quad (16)$$

$$r_i^1(t) = \int_{-\pi}^{\pi} s_i(\theta, t) \exp[i(\theta - \Psi_i(t))] (2\pi)^{-1} d\theta, \quad (17)$$

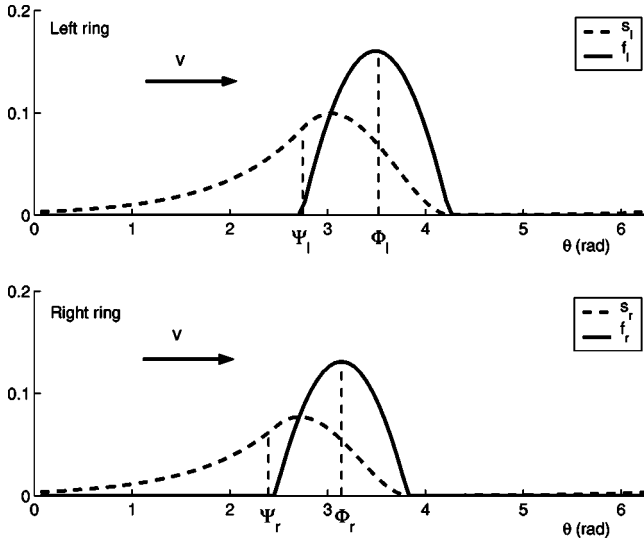


FIG. 4. A snapshot of the traveling bumps in two rings. The dashed lines denote the synaptic variables and the solid lines represent the firing rate.  $\Psi_l$  and  $\Psi_r$  are the phases of the second-order Fourier components of  $s_l(\theta)$  and  $s_r(\theta)$ , respectively. The phase variable  $\Phi_l$  is defined by the peak location of  $f_l(\theta)$ , and  $\Phi_r$  is the peak location of  $f_r(\theta)$ .

where  $i=l,r$  is the index of the left and right rings.  $r_i^0$  represents the mean synaptic activation of neurons in each ring. The phase  $\Psi_i(t)$  is used to make  $r_i^1(t)$  a real number, or in other words,  $r_i^1$  is the amplitude of the first Fourier modes and  $\Psi_i(t)$  is the phase (Fig. 4).

In terms of these order parameters, the neural activities Eq. (2) can be written as

$$f_l(\theta, t) = [I_l^0 + I_l^1 \cos(\theta - \Phi_l)]^+, \quad (18)$$

$$f_r(\theta, t) = [I_r^0 + I_r^1 \cos(\theta - \Phi_r)]^+, \quad (19)$$

where

$$I_l^0 = J_0 r_l^0 + K_0 r_r^0 + b_l, \quad (20)$$

$$I_l^1 = J_1 r_l^1 \cos(\Phi_l - \Psi_l - \phi) + K_1 r_r^1 \cos(\Phi_l - \Psi_r + \psi), \quad (21)$$

$$I_r^0 = K_0 r_l^0 + J_0 r_r^0 + b_r, \quad (22)$$

$$I_r^1 = K_1 r_l^1 \cos(\Phi_r - \Psi_l - \psi) + J_1 r_r^1 \cos(\Phi_r - \Psi_r + \phi). \quad (23)$$

The phase variables  $\Phi_l$  and  $\Phi_r$  are the peak of the neural activities in the left and right ring, respectively (see Fig. 4). They satisfy

$$J_1 r_l^1 \sin(\Phi_l - \Psi_l - \phi) + K_1 r_r^1 \sin(\Phi_l - \Psi_r + \psi) = 0, \quad (24a)$$

$$K_1 r_l^1 \sin(\Phi_r - \Psi_l - \psi) + J_1 r_r^1 \sin(\Phi_r - \Psi_r + \phi) = 0. \quad (24b)$$

Denote the half-width of the positive  $f_l(\theta, t)$  domain by  $\theta_l^c$ , and that of the positive  $f_r(\theta, t)$  domain by  $\theta_r^c$ . If  $f_i$  is a rectified bump, we have  $\theta_i^c = \arccos(-I_i^0/I_i^1)$  for  $i=l,r$ . Next we assume  $\theta_l^c$  and  $\theta_r^c$  are given, in which case the original dynamics can be viewed as linear. Based on this, we perform a Fourier transform of the network dynamics Eqs. (1a) and (1b) and derive the dynamics of the order parameters as follows:

$$\tau \dot{r}_i^0 = -r_i^0 + I_i^1(t) f_0(\theta_i^c), \quad (25a)$$

$$\tau \dot{r}_i^1 = -r_i^1 + I_i^1(t) f_1(\theta_i^c) \cos(\Phi_i - \Psi_i), \quad (25b)$$

$$\tau \dot{\Psi}_i = I_i^1(t) f_1(\theta_i^c) \sin(\Phi_i - \Psi_i), \quad (25c)$$

where  $i=l,r$ . Similarly we can write down the dynamics of the higher-order Fourier components. However, the above set of dynamics is decoupled from the higher-order components, and can be solved independently. In particular, we are interested in the traveling bump solutions in both rings, which can be described by

$$r_i^0 = I_i^1(t) f_0(\theta_i^c), \quad (26)$$

$$r_i^1 = I_i^1(t) f_1(\theta_i^c) \cos(\Phi_i - \Psi_i), \quad (27)$$

$$\tau v = \tan(\Phi_i - \Psi_i), \quad (28)$$

where  $v$  is the velocity of the traveling bumps. Given the vestibular input  $\Delta b$ , the moving velocity of the bumps can be determined numerically from the above set of algebraic equations. Let  $\bar{\beta} = \Phi_r - \Psi_l - \psi$ , and  $\theta = \Phi_r - \Psi_r = \Phi_l - \Psi_l = a \tan(\tau v)$ . This set of algebraic equations can be further simplified into a set of four self-consistent equations with unknown variables  $\theta$ ,  $\bar{\beta}$ ,  $\theta_i^c$ , and  $\theta_r^c$ :

$$K_1 r_l^1 \sin(\bar{\beta}) + J_1 r_r^1 \sin(\theta + \phi) = 0, \quad (29a)$$

$$J_1 r_l^1 \sin(\theta - \phi) + K_1 r_r^1 \sin(2\theta - \bar{\beta}) = 0, \quad (29b)$$

$$I_r^1 = K_1 r_l^1 \cos(\bar{\beta}) + J_1 r_r^1 \cos(\theta + \phi), \quad (29c)$$

$$I_l^1 = J_1 r_l^1 \cos(\theta - \phi) + K_1 r_r^1 \cos(2\theta - \bar{\beta}), \quad (29d)$$

where  $I_r^1$ ,  $I_l^1$ ,  $r_l^1$ , and  $r_r^1$  can be written as functions of  $\theta_i^c$  and  $\theta_r^c$ .

$$I_r^1 = [b_r z_l - b_l K_0 f_0(\theta_l^c)] [K_0^2 f_0(\theta_r^c) f_0(\theta_l^c) - z_l z_r]^{-1}, \quad (30a)$$

$$I_l^1 = [b_l z_r - b_r K_0 f_0(\theta_r^c)] [K_0^2 f_0(\theta_l^c) f_0(\theta_r^c) - z_l z_r]^{-1}, \quad (30b)$$

with  $z_i = J_0 f_0(\theta_i^c) + \cos \theta_i^c$  for  $i=l,r$ , and the order parameter  $r_i^1$  can be derived from Eq. (27). Equation (29) can be solved numerically.

### A. Linearity when $J_1=K_1$

One critical requirement on our model to achieve accurate integration is that the velocity of the traveling bumps should be proportional to the vestibular input over all possible ranges of  $\Delta\hat{b}$ . Our simulation study shows that the network achieves excellent linearity when  $J_1=K_1$  (see Fig. 3 for different choices of  $K_1$  and  $J_1$ ). One typical result is shown in Fig. 3(d). Next we present the analysis to justify this result.

As we have stated, the  $v-\Delta\hat{b}$  curve typically follows a sigmoidal shape, saturating on both ends when  $|\Delta\hat{b}|$  is larger than a certain critical value  $\Delta\hat{b}_c$ . To measure the quality of the linearity over the nonsaturated regime of  $\Delta\hat{b}$ , we can simply compare the difference between the slope at the origin and the velocity-input ratio at the critical point,  $v_{sat}/\Delta\hat{b}_c$ .

First, we determine the critical  $\Delta\hat{b}_c$  that gives rise to the saturation velocity. At the critical  $\Delta\hat{b}_c$ , one ring becomes inactive, and with no loss of generality we assume the left ring is inactive, that is,  $r_l^1=0$ ,  $\theta_l^c=0$ . From Eq. (29a), we have  $\theta=-\phi$  and  $\bar{\beta}=2\theta$ , and therefore  $I_r^1=J_1r_r^1$  and  $I_l^1=K_1r_r^1$ . Substituting these into Eq. (30), we find  $\Delta\hat{b}_c$  to be

$$\Delta\hat{b}_c=[(K_0-J_0)f_0(\theta_r^c)+K_1/J_1-\cos\theta_r^c] \times [(J_0+K_0)f_0(\theta_r^c)+K_1/J_1+\cos\theta_r^c]^{-1}, \quad (31)$$

where  $\theta_r^c$  satisfies  $J_1f_1(\theta_r^c)\cos\phi=1$ , from which  $\theta_r^c$  can be determined.

Typically  $\theta_r^c$  can only be solved by numerical methods. However, an approximate value of  $\theta_r^c$  can be found by asymptotic expansion of the function  $f_1(x)\approx x^3/(3\pi)$ . Similarly, the function  $f_0(x)$  can be approximated by  $x^3/(3\pi)$ . Therefore,  $f_0(\theta_r^c)\approx 1/(J_1\cos\phi)$ . Substituting this into Eq. (31), we find

$$\Delta\hat{b}_c\approx[K_0-J_0+J_1\cos\phi(K_1/J_1-\cos\theta_r^c)] \times [J_0+K_0+J_1\cos\phi(K_1/J_1+\cos\theta_r^c)]^{-1}.$$

In our network, the phase variable  $\phi$  is chosen to be close to  $\pi/2$  to get a large saturation velocity, and  $J_0$  is large negative to guarantee the stability of the network. Therefore, the terms containing multiplying  $\cos\phi$  in the above are small and can be neglected in an approximation. After these considerations, the ratio between the velocity and the differential input at the critical value can be approximated by

$$v_{sat}/\Delta\hat{b}_c\approx\tan\phi(J_0+K_0)[\tau(K_0-J_0)]^{-1}. \quad (32)$$

On the other hand, when  $J_1=K_1$ , the slope at the origin derived from Eq. (14) is

$$S_0=2J_1\sin\phi\sin\theta_c\tau^{-1}[-(J_0+K_0)f_0(\theta_c)-\cos\theta_c] \times [\pi-\theta_c(J_0-K_0)]^{-1} \approx\tan\phi\sin\theta_c\tau^{-1}[-(J_0+K_0)\tan\phi][\pi+(J_0-K_0)\theta_c]^{-1} \approx\tan\phi(J_0+K_0)[\tau(K_0-J_0)]^{-1}.$$

In the above approximation, we have used the asymptotic expansion of  $f_0(\theta_c)\approx(2J_1\cos\phi)^{-1}$  and assumed  $|J_0-K_0|\theta_c\gg\pi$ , which holds when  $J_0-K_0$  is large negative. The above result indicates that in this approximation, the  $v-\Delta\hat{b}$  ratio at the critical value is the same as the slope  $S_0$  at the origin. This explains the excellent linearity achieved when  $J_1=K_1$ .

Another requirement on the integration of the head-direction system is that the linearity should cover the entire possible range of  $\Delta\hat{b}$ . From Eq. (32), we have the threshold differential input  $\Delta\hat{b}_c\approx|(K_0-J_0)/(K_0+J_0)|$ . Provided that  $J_0$  is large negative, to guarantee  $\Delta\hat{b}_c>1$ ,  $K_0$  has to be small negative or positive, which implies that the interring global interaction should be weak inhibitory or excitatory. If  $K_0$  is large negative, the saturation happens at a point when  $\Delta\hat{b}<1$  [Fig. 3(c)].

In the following, we consider dynamics for the case  $J_1=K_1$ .

### B. Solution of the network when $J_1=K_1$

When  $J_1=K_1$ , the set of equations used to determine the thresholds and velocity can be simplified. After reordering and simplifying Eq.(29), we find that  $\theta_l^c$ ,  $\theta_r^c$ , and  $\theta$  are determined by

$$f_1(\theta_l^c)\sin(\theta-\phi)+f_1(\theta_r^c)\sin(\theta+\phi)=0, \quad (33)$$

$$J_1f_1(\theta_l^c)\cos\theta\cos(\theta-\phi)+K_1f_1(\theta_r^c)\cos\theta\cos(\theta+\phi)=1, \quad (34)$$

$$[(J_0+K_0)(f_0(\theta_l^c)+f_0(\theta_r^c))+\cos\theta_r^c+\cos\theta_l^c]\Delta\hat{b} = (J_0-K_0)(f_0(\theta_r^c)-f_0(\theta_l^c))+\cos\theta_r^c-\cos\theta_l^c, \quad (35)$$

$\theta$  can be solved for using Eq. (33). Its dependence on  $\theta_l^c$  and  $\theta_r^c$  is given by

$$v=\tan\theta/\tau=\tan\phi[f_1(\theta_l^c)-f_1(\theta_r^c)][\tau(f_1(\theta_l^c)+f_1(\theta_r^c))]^{-1}. \quad (36)$$

Substituting this into Eq. (34), we derive

$$J_1^2[f_1^2(\theta_l^c)+f_1^2(\theta_r^c)+2f_1(\theta_r^c)f_1(\theta_l^c)\cos(2\phi)] = \tan^2\phi[f_1(\theta_l^c)-f_1(\theta_r^c)]^2[f_1(\theta_l^c)+f_1(\theta_r^c)]^{-2}+1.$$

The above and Eq. (35) consists of two self-consistent equations, from which the threshold widths  $\theta_l^c$  and  $\theta_r^c$  can be

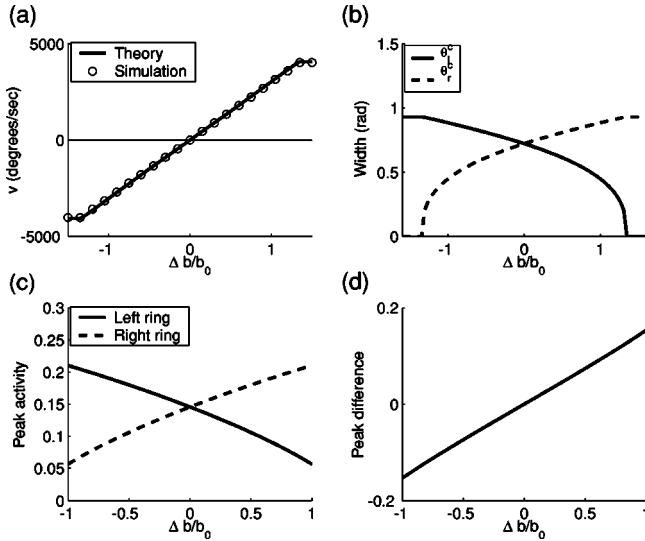


FIG. 5. Results from the theoretical calculations when  $J_1 = K_1$ . The velocity of the traveling bumps as a function of the input is plotted in (a), which verifies the theoretical and the simulation results. The width of the tuning curves are shown as a function of the input in (b). The peak firing rates of the two bumps are modulated by  $\Delta b$ , with the peak rate for each ring shown in (c) and the difference between them shown in (d).

determined for each differential input  $\Delta \hat{b}$ . Using Eq. (36), we can then determine the velocity of the moving bumps for each  $\Delta \hat{b}$ .

The results of this calculation are shown in Fig. 5(a) and are compared with the simulation results, which verify the theoretical calculations.

The threshold widths  $\theta_l^c$  and  $\theta_r^c$  characterize the width of the tuning curves of the head directions. Its dependence on the head moving velocity can be measured experimentally. We plot the change of them as a function of  $\Delta \hat{b}$  in Fig. 5(b) obtained from the above calculation. Besides threshold width, another characterization of the neural responses is the peak firing rates of the traveling bumps in each ring, which can be written as

$$P_r = I_r^1 (1 - \cos \theta_r^c), \quad (37)$$

$$P_l = I_l^1 (1 - \cos \theta_l^c), \quad (38)$$

for the right and left ring, respectively. Here,

$$\begin{aligned} I_r^1 &= I_l^1 \\ &= 2\Delta b \{ (K_0 - J_0) [f_0(\theta_r^c) - f_0(\theta_l^c)] \\ &\quad + \cos \theta_l^c - \cos \theta_r^c \}^{-1}. \end{aligned}$$

The result is plotted in Fig. 5(c), 5(d). It shows that  $P_r$  and  $P_l$  are approximately linearly related to the differential input  $\Delta \hat{b}$ .

## V. STABILITY

The network is translation invariant. There are potential homogeneous solutions. Assume  $s_l(\theta) = u_l$  and  $s_r(\theta) = u_r$ , and substitute them into Eq. (1). We find  $u_l = J_0 u_l + K_0 u_r + b_l$  and  $u_r = J_0 u_r + K_0 u_l + b_r$ , which leads to the homogeneous solutions

$$u_r = b_0 (1 - J_0 - K_0)^{-1} + \Delta b (1 - J_0 + K_0)^{-1}, \quad (39)$$

$$u_l = b_0 (1 - J_0 - K_0)^{-1} - \Delta b (1 - J_0 + K_0)^{-1}. \quad (40)$$

If  $J_0 + K_0 < 1$ , then  $u_r$  and  $u_l$  are both positive, so the homogeneous solutions exist.

Our network works in a regime where a stationary bump develops when  $\Delta b = 0$  and moves when  $\Delta b \neq 0$ . To guarantee that the network works in such a regime, we have to choose synaptic parameters such that the homogeneous solution becomes unstable.

The stability of the homogeneous solution can be easily characterized by perturbing the dynamics around the homogeneous solution. In terms of the first two Fourier components, the perturbed dynamics can be written as

$$\tau \delta \dot{r}_l^0 = (J_0 - 1) \delta r_l^0 + K_0 \delta r_r^0, \quad (41)$$

$$\tau \delta \dot{r}_r^0 = (J_0 - 1) \delta r_r^0 + K_0 \delta r_l^0, \quad (42)$$

for the first Fourier component, and

$$\tau \delta \dot{r}_l^1 = (J_1/2 \cos \phi - 1) \delta r_l^1 + K_1/2 \cos \phi \delta r_r^1, \quad (43)$$

$$\tau \delta \dot{r}_r^1 = (J_1/2 \cos \phi - 1) \delta r_r^1 + K_1/2 \cos \phi \delta r_l^1, \quad (44)$$

for the second Fourier component. The condition for Eqs. (41) and (42) to be stable is  $J_0 + |K_0| < 2$ . This is typically satisfied if we choose  $J_0$  to be large negative. For  $r_l^1$  and  $r_r^1$  to be stable requires that  $J_1 \cos \phi < 1$ , provided that  $J_1 = K_1$  as we have constrained. Therefore, to break the stability of the homogeneous solution, we can choose  $J_1 > 1/\cos \phi$ .

The stability of the stationary bump or traveling bumps can be analyzed by perturbing the dynamics defined by Eq. (25) around the stationary or traveling bump solutions. The perturbed dynamics involves many terms, and the details are not included in this paper. The phase diagram of solutions when  $\Delta \hat{b} = 0$  obtained from simulation is shown in Fig. 6. This phase diagram does not include all possible solutions among all range of synaptic parameters. For example, if we choose parameters such that  $K_1 < J_1 \sin \phi$ , the stationary bump solution will not exist and the network will yield a lurching bump solution whose shape changes in time. For the stability of the traveling bump solutions when  $\Delta \hat{b} \neq 0$ , the bifurcation line from the homogeneous solution is the same as the one shown in Fig. 6, but the boundary where the traveling bump solution diverge is different for different  $\Delta \hat{b}$ .

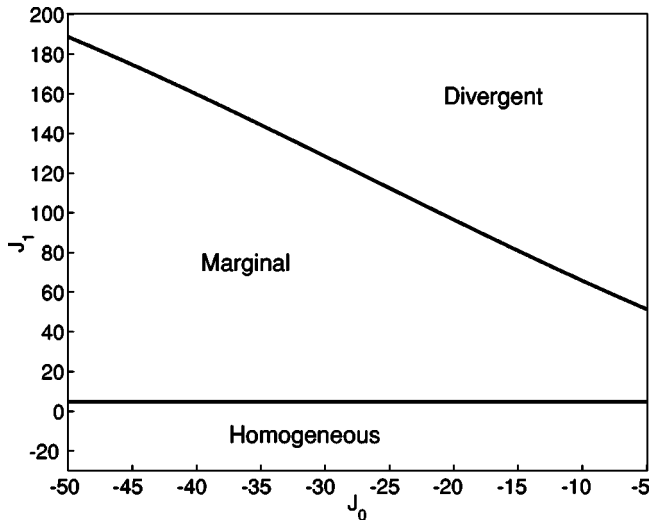


FIG. 6. Phase diagram when  $\Delta b = 0$ ,  $K_1 = J_1$ , and other parameters  $K_0 = -5$ ,  $\phi = 80^\circ$ , and  $\psi = 50^\circ$ . The marginal phase is the desired parameter regime, in which a stationary bump develops, although the location of the bump can be arbitrary.

## VI. ADT AND POS HEAD-DIRECTION CELLS

Head-direction cells have been found in many brain areas, each having different tuning properties. Lesion studies and anatomical evidence suggest that the core attractor network of the head-direction system is located in the lateral mammillary nucleus (LMN) and dorsal tegmental nucleus (DTN), whereas downstream nuclei such as ADT and POS receive feedforward input from the attractor network [10,11].

As shown in the preceding sections, the activities of neurons in the double-ring network are not only tuned to head direction, but modulated by head velocity also (see Fig. 5c,d), which is consistent with the properties of cells found in LMN and DTN [12,13].

Head-direction cells in two downstream nuclei ADT and POS have very different tuning properties. During head movement, tuning curves in ADT are usually skewed with preferred directions tilted toward the directions in the future. In contrast, POS cells usually have similar tuning curves, irrespective of the directions of head movement [14,15].

Let us assume ADT and POS read out responses from the double-ring network. Two simple readout schemes are the average and maximum of the activities in the two rings. Next, we analyze these two simple readout methods of the firing rates  $f_l$  and  $f_r$ . We find that the two readout methods can indeed approximate response behavior resembling that of ADT and POS neurons [14–16,6,7].

Suppose ADT cells read out activities of the double ring using a maximum operation,  $z(\theta) = \max(f_r(\theta), f_l(\theta))$  (see Fig. 7). Recall that there is an activity offset between the two rings [cf. Eq. (5)]. When the head rotates counterclockwise, the activity on the left ring is larger than the activity on the right ring, so the tuning of  $z(\theta)$  is biased to the right. Similarly, for clockwise turns,  $z(\theta)$  is biased to the left. In either cases, the tuning curve is skewed toward head directions in the future, which could be a mechanism for anticipatory coding.

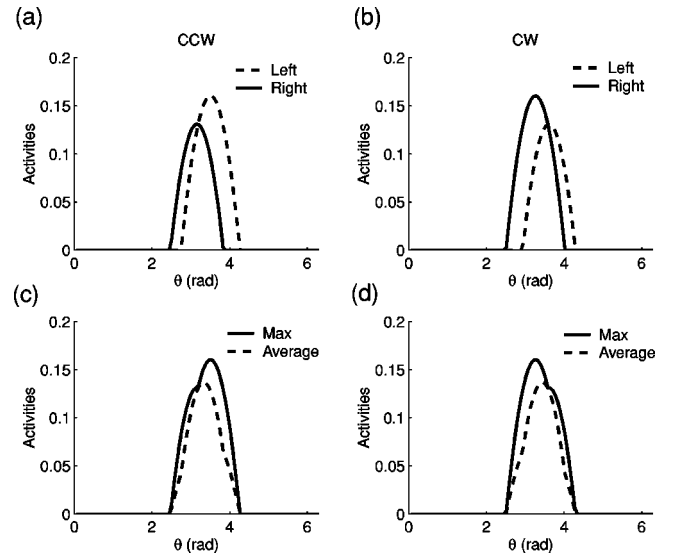


FIG. 7. Snapshots of the activities on the two rings for counterclockwise (CCW) head rotation (a) and clockwise rotation (CW) (b), respectively. Reading out the activities by averaging and by a maximum operation (c, d).

Suppose POS cells read out activities of the double ring using an averaging operation,  $y(\theta) = 1/2[f_r(\theta) + f_l(\theta)]$  (Fig. 7). In contrast to those of ADT cells, the tuning curves of POS cells are not significantly biased toward either directions, because averaging is a symmetric operation and all information about the direction of head rotations is lost.

## VII. DISCUSSION ON SYNAPTIC PARAMETERS

Here we discuss how the various connection parameters contribute to the double-ring network to function as an integrator. In particular, we discuss how parameters have to be tuned for proper integration to occur over a large  $\Delta b$  and in  $v$ .

(i)  $\tau$ : By assumption the synaptic time constant  $\tau$  is large.  $\tau$  has the simplest effect of all parameters on the integrator properties. According to Eq. (14),  $\tau$  scales the range of  $v$ . Notice that if  $\tau$  were small, a large range of  $v$  could be trivially achieved. We show here how to achieve proper integration with large  $\tau$ .

(ii)  $\phi$ : The connection offset  $\phi$  between neurons receiving similar vestibular input is the sole parameter besides  $\tau$  that determines the saturating head velocity, beyond which integration is impossible. According to Eq. (15), the saturating velocity is large if  $\phi$  is close to  $90^\circ$  (we want the saturating velocity to be large). In other words, for good integration, excitatory connections should be strongest (or inhibitory connections weakest) for neuron pairs with preferred head directions differing by a little less than  $90^\circ$ .

(iii)  $\psi$ : The connection offset  $\psi$  between neurons receiving different vestibular input only affects the shift in activity profiles of the two rings. It determines how much the tuning curves of the ADT head-direction cells are tilted, that is, the anticipatory time of the ADT cells.

(iv)  $K_0$  and  $K_1$ : The interring connections should be mainly weak inhibitory, or excitatory, which implies that  $K_0$  should not be too negative. The intuitive reason is the following. We want the integration to be as linear in  $\Delta b$  as possible, which means that we want our linear expansions Eqs. (9) and (10) to deviate as little as possible from Eq. (4). Hence, the differential gain between the two rings should be small, which is the case when the two rings excite each other. The interring excitation makes sure, even for large values of  $\Delta b$ , that there are comparable activity levels on the two rings. This is one of the main points of this study.

(v)  $J_0$  and  $J_1$ : The intraring connections should be mainly inhibitory, which implies that  $J_0$  should be strongly negative. The reason for this is that inhibition is necessary to result in proper and stable integration. Since inhibition cannot come from the interring connections, it has to come from  $J_0$ . Notice also that according to Eq. (7),  $J_1$  cannot be much larger than  $K_1$ . If  $J_1 > K_1 / \sin \phi$ , the model cannot model the persistent activities for no head-movement case.

### VIII. CONCLUSION AND REMARKS

We have presented a different model for neural integration in the head-direction system with potentially slow synapses. The model is essentially a push-pull model with two populations of neurons receiving differential vestibular inputs. The difference in input breaks the balance between the interactions of two rings that is maintained during stationary head states, and causes activity bump developed in both rings to

move around. With carefully chosen synaptic parameters, we demonstrate that the integration can be achieved with high precision.

Synapses with slow dynamics are important for attractor models described here or previously. There are two reasons for this. First, all the attractor models are described in terms of firing rate of neurons. These rate model dynamics can be derived from spiking neuronal dynamics using the method of averaging [17], which is valid only for slow synapses. Second, it has been shown that the directional tuning properties of head-direction cells can be maintained in the dark for several minutes, which contrasts significantly with the time constant of individual synapses, which is in the order of 1 ms for fast and 100 ms for slow synapses. This requires that synaptic connection parameters of the attractor models need to be precisely tuned. Slow synapses weaken the precise tuning requirement.

The head-direction system is also influenced significantly by visual landmarks [18]. It is believed that the visual input is used to calibrate the directional heading, and also works as a feedback signal to adjust synaptic parameters for achieving accurate integration. We are currently investigating learning rules that use the visual feedback to tune synaptic parameters. The results will be reported elsewhere.

### ACKNOWLEDGMENTS

We acknowledge helpful discussions with Dr. M. Goldman.

- 
- [1] H. Blair, P. Sharp, and J. Cho, *Trends Neurosci.* **24**, 289 (2001).
- [2] H. Blair and P. Sharp, *J. Neurosci.* **15**, 6260 (1995).
- [3] H. Blair, J. Cho, and P. Sharp, *Neuron* **21**, 1387 (1998).
- [4] R. Stackman and J. Taube, *J. Neurophysiol.* **18**, 9020 (1998).
- [5] K. Zhang, *J. Neurosci.* **16**, 2112 (1996).
- [6] A. Redish, A.N. Elga, and D. Touretzky, *Network: Comput. Neural Syst.* **7**, 671 (1996).
- [7] J. Goodridge and D. Touretzky, *J. Neurophysiol.* **83**, 3402 (2000).
- [8] H. Blair, B. Lipscomb, and P. Sharp, *J. Neurophysiol.* **78**, 145 (1997).
- [9] D. Hansel and H. Sompolinsky, in *Methods in Neuronal Modeling*, edited by C. Koch and I. Segev (MIT Press, Cambridge, MA, 1998), pp. 499–567.
- [10] J.S. Taube, J.P. Goodridge, E.J. Golob, P.A. Dudchenko, and R.W. Stackman, *Brain Res. Bull.* **40**, 477 (1996).
- [11] H.T. Blair, J. Cho, and P.E. Sharp, *J. Neurosci.* **19**, 6673 (1999).
- [12] P.E. Sharp, A. Tinkelman, and J. Cho, *Behav. Neurosci.* **115**, 571 (2001).
- [13] R.W. Stackman and J.S. Taube, *J. Neurosci.* **18**, 9020 (1998).
- [14] H.T. Blair and P.E. Sharp, *J. Neurosci.* **15**, 6260 (1995).
- [15] H.T. Blair, B.W. Lipscomb, and P.E. Sharp, *J. Neurophysiol.* **78**, 145 (1997).
- [16] J.S. Taube, R.U. Muller, and J.B. Ranck, *J. Neurosci.* **10**, 420 (1990).
- [17] B. Ermentrout, *Neural Comput.* **6**, 679 (1994).
- [18] J.S. Taube, R.U. Muller, and J.B. Ranck, *J. Neurosci.* **10**, 436 (1990).